Geophysical Journal International

Geophys. J. Int. (2017) **211,** 1601–1612
Advance Access publication 2017 September 20
GJI Marine geosciences and applied geophysics

doi: 10.1093/gji/ggx395

Tsunamis from strike-slip earthquakes in the Wharton Basin, northeast Indian Ocean: March 2016 M_w7.8 event and its relationship with the April 2012 M_w 8.6 event

Mohammad Heidarzadeh,[1] Tomoya Harada,[2] Kenji Satake,[2] Takeo Ishibe[3] and Tomohiro Takagawa[4]

[1]*Division of Civil Engineering, Department of Mechanical, Aerospace and Civil Engineering, Brunel University London, Uxbridge UB8 3PH, United Kingdom. E-mail: mohammad.heidarzadeh@brunel.ac.uk*
[2]*Earthquake Research Institute, The University of Tokyo, Tokyo 113-0032, Japan*
[3]*Association for the Development of Earthquake Prediction, Tokyo 101-0064, Japan*
[4]*Port and Airport Research Institute, Yokosuka 239-0826, Japan*

Accepted 2017 September 19. Received 2017 September 14; in original form 2016 December 3

SUMMARY

The Wharton Basin, off southwest Sumatra, ruptured to a large intraplate left-lateral strike-slip M_w 7.8 earthquake on 2016 March 2. The epicentre was located ~800 km to the south of another similar-mechanism intraplate M_w 8.6 earthquake in the same basin on 2012 April 11. Small tsunamis from these strike-slip earthquakes were registered with maximum amplitudes of 0.5−1.5 cm on DARTs and 1−19 cm on tide gauges for the 2016 event, and the respective values of 0.5−6 and 6−40 cm for the 2012 event. By using both teleseismic body waves and tsunami observations of the 2016 event, we obtained optimum slip models with rupture velocity (V_r) in the range of 2.8–3.6 km s^{-1} belonging to both EW and NS faults. While the EW fault plane cannot be fully ruled out, we chose the best model as the NS fault plane with a V_r of 3.6 km s^{-1}, a maximum slip of 7.7 m and source duration of 33 s. The tsunami energy period bands were 4−15 and 7−24 min for the 2016 and 2012 tsunamis, respectively, reflecting the difference in source sizes. Seismicity in the Wharton Basin is dominated by large strike-slip events including the 2012 (M_w 8.6 and 8.2) and 2016 (M_w 7.8) events, indicating that these events are possible tsunami sources in the Wharton Basin. Cumulative number and cumulative seismic-moment curves revealed that most earthquakes are of strike-slip mechanisms and the largest seismic-moment is provided by the strike-slip earthquakes in this basin.

Key words: Tsunamis; Indian Ocean; Fourier analysis; Numerical modelling; Earthquake source observations; Seismicity and tectonics.

1 INTRODUCTION

A large strike-slip earthquake occurred within the Wharton Basin, offshore southwest of Sumatra, Indonesia on 2016 March 2. The moment magnitude, M_w, was reported as 7.8 with an epicentre located at 94.330°E and 4.952°S and a depth of 24.0 km by the United States Geological Survey (USGS) (red star in Fig. 1). The origin time was 12:49:48 UTC. A small tsunami was generated following the 2016 earthquake with zero-to-peak amplitude of up to 19 cm on the examined tide gauge stations (Fig. 1d). Deep-ocean Assessment and Reporting of Tsunami (DART) gauges recorded amplitudes up to 1.5 cm (Fig. 1d). Lay *et al.* (2016) used seismic records of the 2016 earthquake and reported a bilateral rupture on a NS-striking fault dipping eastward with a velocity of $\leq$ 2 km s^{-1} and duration of ~35 s. Gusman *et al.* (2017) applied a joint teleseismic-tsunami inversion to propose a NS-striking fault dipping westward with a rupture velocity of 2.0 km s^{-1}. The 2016 earthquake occurred ~800 km to the south of the twin large strike-slip earthquakes on 2012 April 11 (M_w 8.6 and 8.2 with around two hours of time intervals, Fig. 1). The 2012 M_w 8.6 event was the largest ever-recorded intraplate earthquake (Yue *et al.* 2012). The rupture pattern of the 2012 M_w 8.6 earthquake consisted of several orthogonal faults (Meng *et al.* 2012; Satriano *et al.* 2012; Wang *et al.* 2012; Wei *et al.* 2013); making this event as one of the most complex ruptures ever recorded. The Warton Basin ruptured to other large strike-slip earthquakes in 1928 (M_w 7.7), in 1949 (M_w 6.8), and in 2000 (M_w 7.9) (Fig. 1).

While giant/great earthquakes are typical of subduction plate boundaries characterized by thrust-fault mechanisms, occurrence of the large intraplate strike-slip earthquakes off Sumatra have attained significant attention in the scientific community (Abercrombie *et al.* 2003; Duputel *et al.* 2012; Yue *et al.* 2012; Wei *et al.* 2013; Aderhold & Abercrombie 2016; Gusman *et al.* 2017). The epicentral area of the aforesaid earthquakes is named as the Wharton

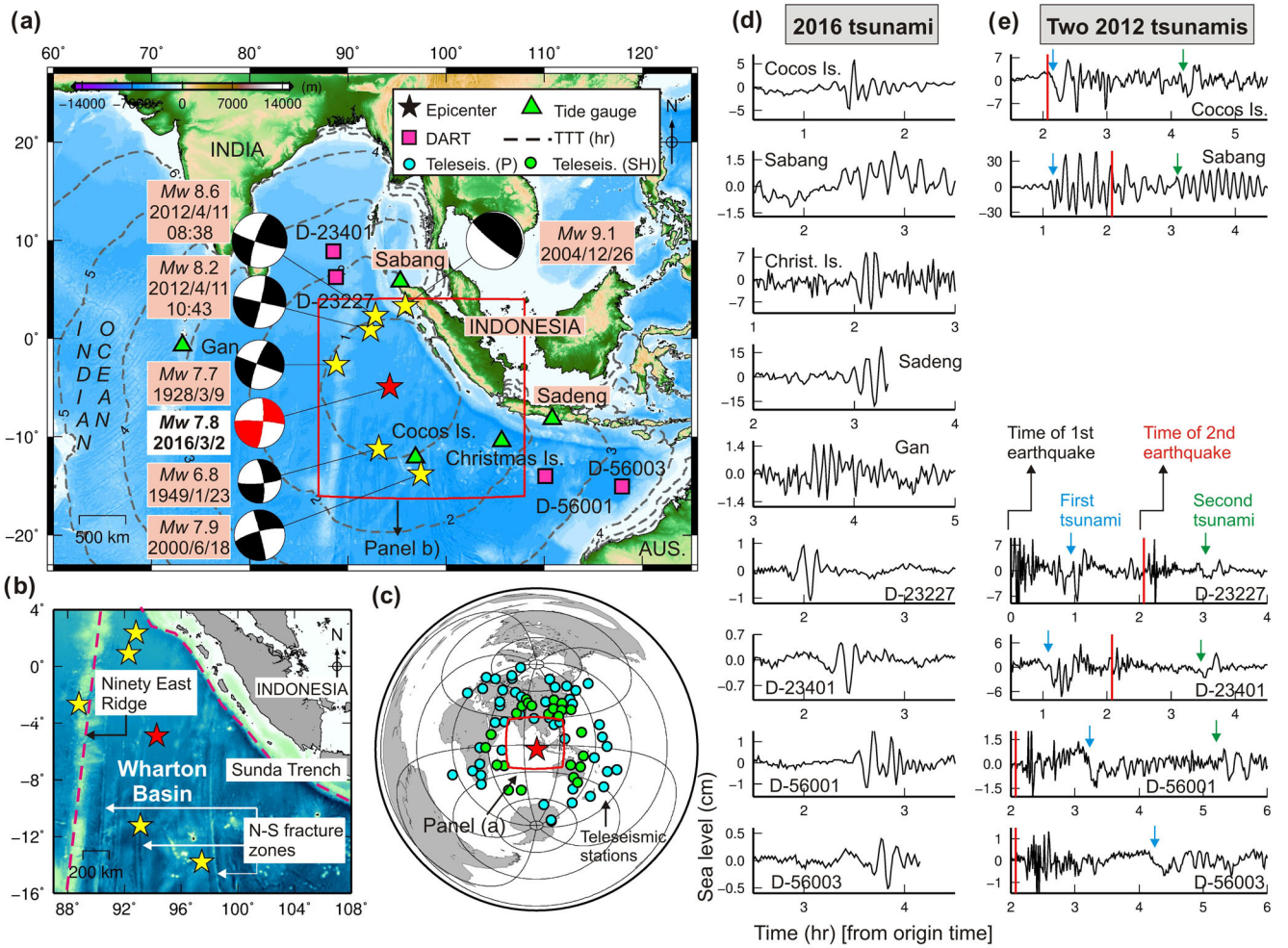

Figure 1. (a) Epicentres and mechanisms of the large strike-slip intraplate earthquakes in the Wharton Basin along with the locations of the DART and tide gauge stations used in this study. Focal mechanisms are from GCMT catalogue. The focal mechanisms for the 1928 and 1949 are from Petroy & Wiens (1989). *TTT* stands for tsunami travel time. (b) Inset showing the tectonic and bathymetric features along with north–south trending fracture zones. (c) Teleseismic stations used in this study to analyse the 2016 earthquake including both *P* (cyan circles) and *SH* (green circles) waves. (d,e) Tsunami waveforms for the 2012 and 2016 tsunamis, respectively.

Basin, located between the Sunda Trench to the east and the Ninety East Ridge to the west including several north–south (NS) trending fracture zones (Fig. 1b). The strike-slip seismicity in the Wharton Basin can be attributed to the activities of these fracture zones (Abercrombie *et al.* 2003; Wiseman & Burgmann 2012). Analysis of seismic profiles from the Wharton Basin revealed active left-lateral NS strike-slip faults (Deplus *et al.* 1998; Qin & Singh 2015).

The purpose of this study is to understand the tsunamigenic potential of large strike-slip earthquakes in the Wharton Basin by investigating the March 2016 and April 2012 events. In this context, we employed teleseismic and tsunami observations of the 2016 off Sumatra event and applied teleseismic body wave inversions and forward tsunami simulations to infer the source slip distribution. Then, we compared the tsunami waveforms and spectral properties of the 2016 and 2012 events. Finally, seismicity analysis was employed to shed some lights on the seismicity pattern in the Wharton Basin.

2 METHODS AND DATA

We first applied teleseismic body wave inversion in order to estimate the slip distribution of the earthquake; then employed forward tsunami simulations using the inverted slip distributions in order to examine the agreement between observed and simulated tsunami waveforms (Heidarzadeh *et al.* 2015). To characterize the tsunami waves, we performed Fourier analysis. Finally, we conducted seismicity analysis in order to analyse the seismicity pattern in the Wharton Basin. The data used here were 87 teleseismic body waves (63 *P*-waves and 24 *SH* waves) (Fig. 1c) and nine sea level records (four DART and five tide gauge records) (Fig. 1) as well as earthquake catalogue by Global Centroid-Moment-Tensor Project (GCMT).

Teleseismic inversion was conducted by applying the Kikuchi & Kanamori's (1991) method to the vertical components of the far-field *P* and *SH* waves (at distances between 30° and 100° from the source) which were bandpass filtered in the range of 0.004–1.0 Hz. We used GCMT focal mechanism solution for this earthquake as strike = 5° and dip = 90°. We examined both NS and east–west (EW) striking fault planes for two reasons: first the aftershocks are sparse and are not conclusive; second, the Wharton Basin has past experience of rupturing on both NS- and EW-striking faults (e.g. Meng *et al.* 2012). Subfaults with dimensions of 10 km (along strike) × 8 km (along dip) were used for teleseismic inversion allowing each subfault to rupture for a maximum duration of 7.5 s

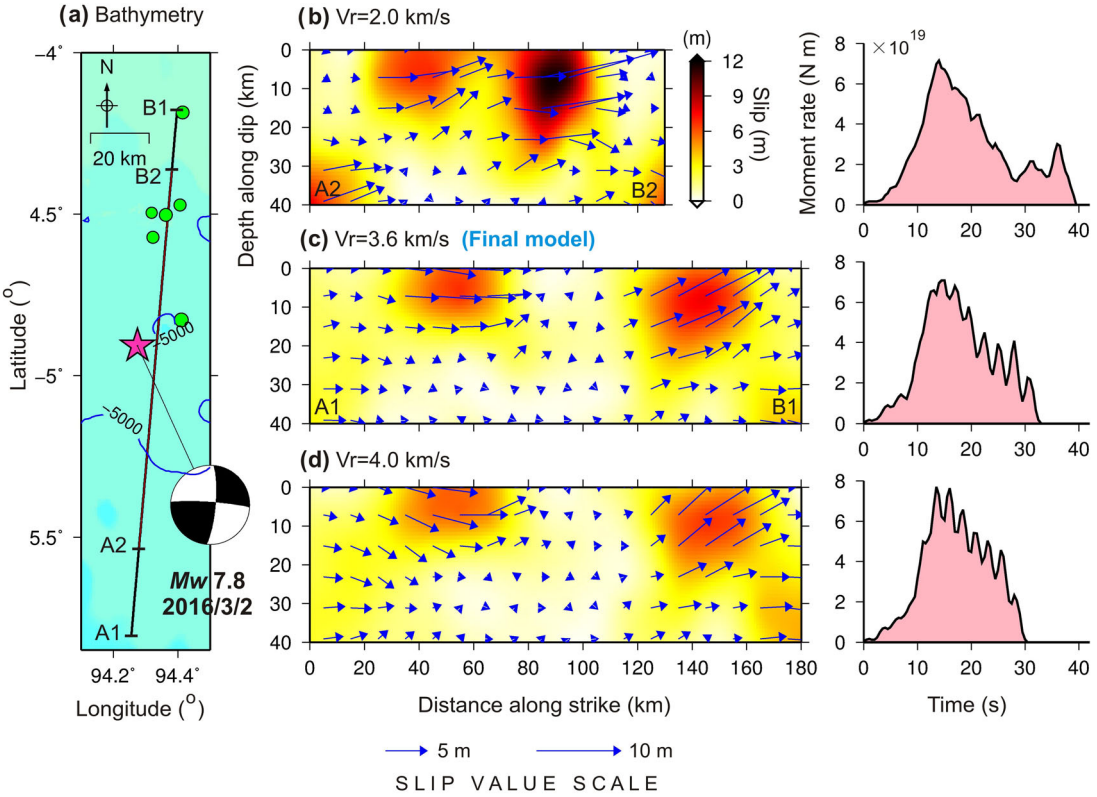

Figure 2. Results of teleseismic body wave inversions using different rupture velocities for the north–south striking fault. (a) Bathymetry and location of the fault. Blue contours are the 5000 m water depth contour. (b–d) From left to right: slip distribution and source–time (moment-rate) function for various models having $V_r = 2.0$, 3.6 and 4.0 km s^{-1}, respectively. Green circles show one-week aftershocks.

using four rise-time triangles; each having 3 s duration and 1.5 s of overlaps between them. Teleseismic inversions were performed for thirteen rupture velocities (V_r) from 1.6 to 4.0 km s^{-1} with 0.2 km s^{-1} intervals for both NS and EW-striking fault planes. Slip distributions were obtained for each V_r. The purpose was to examine which fault plane (i.e. NS- or EW-striking plane) and which slip distribution better reproduce the tsunami observations. We mention here that what makes the difference in simulated tsunami waveforms is not rupture velocity itself but the slip distribution estimated by teleseismic waveform inversion assuming different rupture velocity (e.g. Gusman *et al.* 2015).

Nonlinear shallow water model of Satake (1995) was applied for tsunami simulations using 30 arc-sec bathymetry data of GEBCO (Intergovernmental Oceanographic Commission *et al.* 2003). We utilized a time step of 1.0 s in our nonlinear simulations. Crustal deformation was calculated using Okada (1985) formula. Normalized Root Mean Square (NRMS) misfit was used to quantify the match between observations and simulations (Heidarzadeh *et al.* 2016a). We applied the averaged modified-periodogram method of Welch (1967) for Fourier analysis using 2 hr long segment of the tsunami waveforms and considering Hamming window and 50 per cent of overlaps (e.g. Heidarzadeh & Satake 2014). Geoware's (2011) software was used for tsunami travel time analysis.

3 SOURCE MODEL OF THE MARCH 2016 OFF SUMATRA EARTHQUAKE

Results of teleseismic inversions for NS- and EW-striking faults using different V_r are shown in Figs 2 and 3, respectively. The teleseismic waveform-fits between the observed and synthetic waveforms are shown in Supporting Information Figs S1–S3 for three cases of $V_r = 2.0$, 3.6 and 4.0 km s^{-1} for the NS fault. It can be seen that the waveform-fits look similar for different models. The teleseismic NRMS misfits were 0.563, 0.573 and 0.577 for the aforesaid models, respectively, and the NRMS misfit considering all models for both NS and EW faults is almost a horizontal line (filled-black and open-red circles in Fig. 3e). The source-time functions indicate that the rupture duration decreases from 40 s for model $V_r = 2$ km s^{-1} to 30 s for model $V_r = 4$ km s^{-1} (Figs 2–4). A trade-off can be seen among V_r, source duration and NRMS (Fig. 4): by increasing V_r, source duration decreases whereas NRMS increases. Although the waveform-fits and NRMS are very close to each other for all models, Figs 2 and 3 show that the maximum slip decreases and the slip area expands by increasing the rupture velocity. In other words, although the slip distributions are different (Figs 2 and 3), the teleseismic waveform-fits remain similar for various models (Fig. 3e) which makes it difficult to choose the best slip model among the 26 source models. Therefore, we performed tsunami simulations using the 26 slip models obtained from teleseismic inversions for both NS and EW faults (Figs 5 and 6 and Supporting Information Fig. S4).

Tsunami simulations showed that the simulated waves are significantly different from one model to another at some stations (Figs 5 and 6 and Supporting Information Fig. S4). For instance, the simulated tsunami amplitudes at Cocos Island for model $V_r = 2$ km s^{-1} (Fig. 5a) is more than twice larger than that for model $V_r = 4.0$ km s^{-1} (Fig. 5c). For DART records of 23227 and 23401, the simulated waveforms from the NS fault with $V_r = 2$ km s^{-1} lack the first elevation wave (Fig. 5a) whereas it is clear in models $V_r = 3.6$ and 4 km s^{-1} (Figs 6b and c). NRMS misfits for tsunami simulations vary in a wide range whereas they are almost on a horizontal line

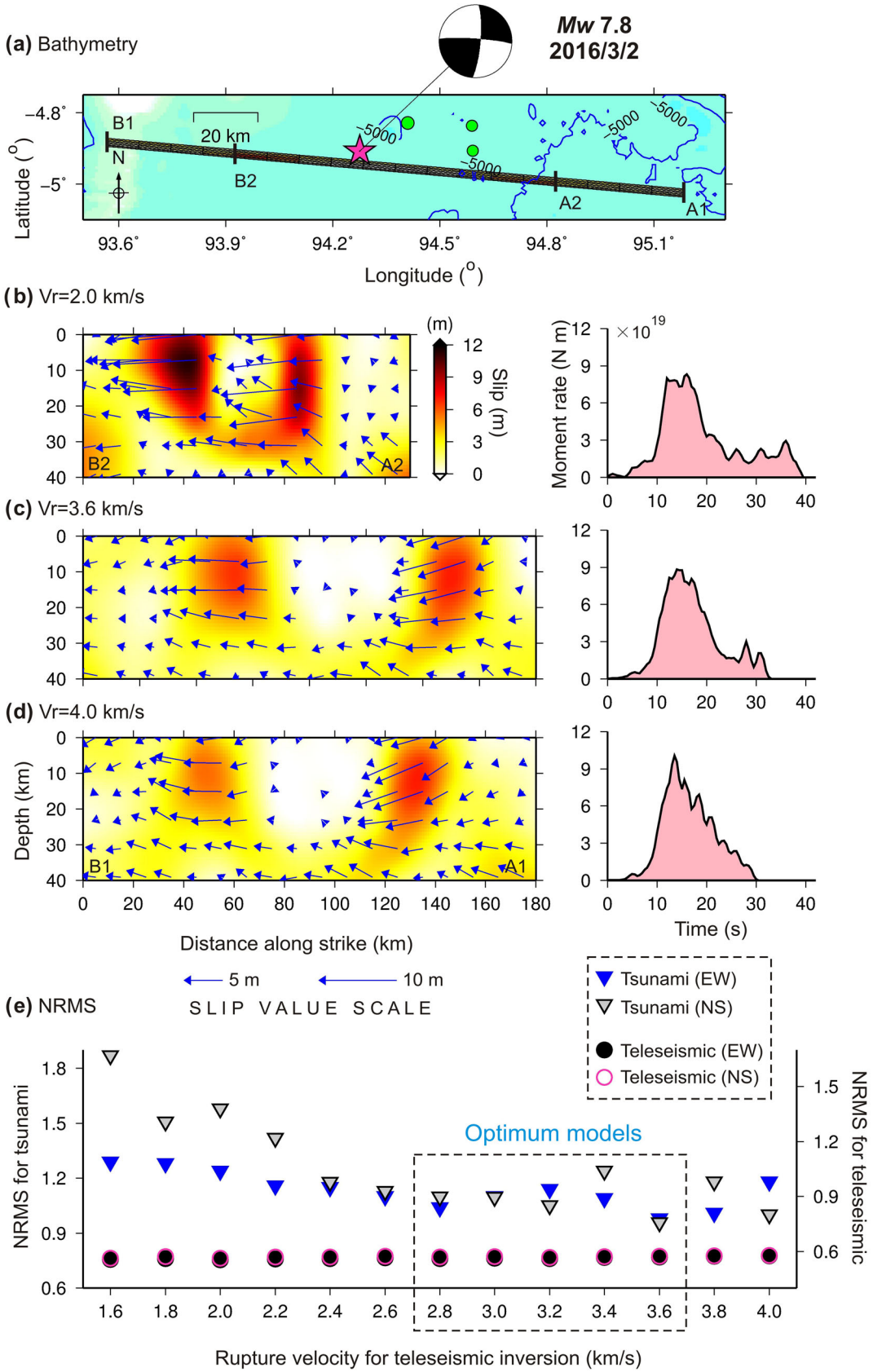

Figure 3. Results of teleseismic body wave inversions using different rupture velocities for the east–west striking fault. (a) Bathymetry and location of the fault. Blue contours are the 5000 m water depth contour. (b–d) From left to right: slip distribution and source–time (moment-rate) function for various models having $V_r = 2.0$, 3.6 and 4.0 km s^{-1}, respectively. Green circles show one-week aftershocks. (e) Normalized root-mean-square misfits for teleseismic and tsunami results for both NS and EW faults and for various source models.

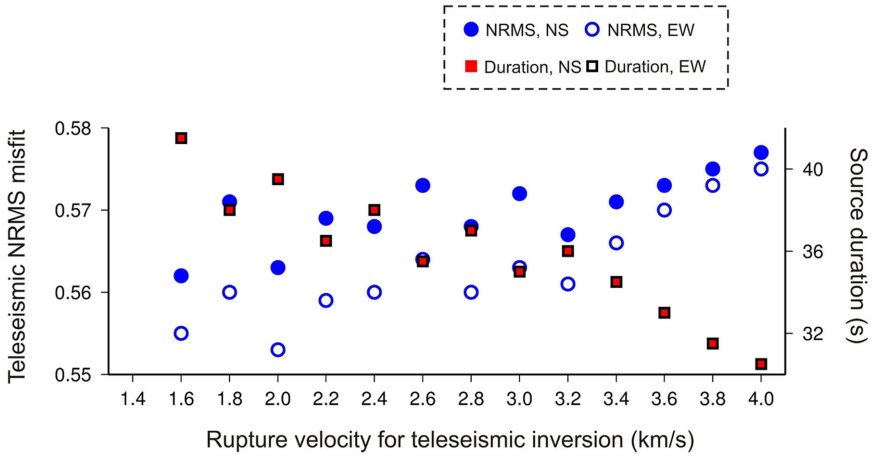

Figure 4. Trade-off among rupture duration, rupture velocity and teleseismic NRMS misfits.

for teleseismic inversions (Fig. 3e). The tsunami NRMS misfits of the NS fault for the three models of $V_r = 2.0$, 3.6 and 4.0 km s^{-1} are 1.58, 0.96 and 1.0, respectively. The respective values for the EW fault are: 1.24, 0.98 and 1.18. EW models are better at velocities of 1.6, 1.8, 2.0, 2.2, 2.8, 3.4 and 3.8 km s^{-1} while the NS models produce better fits at 3.0, 3.2, 3.6 and 4.0 km s^{-1}. Tsunami simulations for both NS- and EW-striking faults point to the model $V_r = 3.6$ km s^{-1} as the best model with similar NRMS misfits. Because the differences in tsunami NRMS misfits is small for both NS and EW faults in the range of $V_r = 2.8$–3.6 km s^{-1}, these models are named as optimum models in Fig. 3(e). It is difficult to choose the best model or best fault plane out of the current results. The NS-striking fault gives good simulation results at DARTs 23401, 56001 and 56003 (Fig. 5b); the EW-striking fault produces better results in Cocos Is., and DARTs 23227 and 23401 (Fig. 6b). Lack of resolution to clearly distinguish between the NS and EW faults can be attributed to the small size of the tsunami and the sparse distribution of the tsunami gauges. We pick the model $V_r = 3.6$ km s^{-1} from the NS-striking fault (Figs 2c and 5b) as the best model because it is the optimum point in tsunami NRMS plot (Fig. 3e) for both earthquake and tsunami data. The maximum and average slips of this model are 7.7 and 2.3 m, respectively (Fig. 3c). Source duration is 33 s and the peak of the source-time function occurs at 15 s.

The optimum rupture velocity of 2.8–3.6 km s^{-1} for this intraplate strike-slip earthquake (Fig. 3e) confirms previous results by Heidarzadeh *et al.* (2016b) that intraplate earthquakes tend to have higher V_r (>2.0 km s^{-1}) compared to interplate events (<2.0 km s^{-1}). Although the rupture duration, source-time function and rupture dimensions reported here fairly agree with those reported by Lay *et al.* (2016) and Gusman *et al.* (2017), our optimum V_r of 2.8–3.6 km s^{-1} is higher than that of $V_r \leq 2$ and $V_r = 2$ km s^{-1} by Lay *et al.* (2016) and Gusman *et al.* (2017), respectively. This is possibly due to different datasets and methods used in these studies. We used a combination of seismic and tsunami observations whereas Lay *et al.* (2016) relied solely on seismic data. In addition, we applied forward tsunami modelling while Gusman *et al.* (2017) applied joint inversion of seismic and tsunami waveforms. It is natural that different methods result in different V_r values as it was the case for the 2011 off-Tohoku (Japan) M_w 9.0 earthquake where a V_r in the range of 1.2−4 km s^{-1} was reported by different authors (Heidarzadeh *et al.* 2016b). A detailed sensitivity analysis by Gusman *et al.* (2017, fig. S12) showed that the NRMSs are generally smaller for larger V_r if the weights for tsunami data are larger or smaller than their choice in the joint inversion. Our largest slip value of 7.7 m is close to that of 9 m reported by Gusman *et al.* (2017), but is smaller to the respective value ∼13 m by Lay *et al.* (2016). The match between simulated and observed tsunami waveforms is not as good as those achieved in other studies for tsunamigenic thrust earthquakes. This could be attributed to several factors such as (1) strike-slip earthquakes produce smaller seafloor vertical deformation compared to similar-size thrust events, and (2) initial seafloor deformation due to strike-slip events is more complicated as it includes four poles of uplift and subsidence whereas it is usually dipole for thrust events.

4 COMPARISON OF THE 2012 AND 2016 OFF SUMATRA TSUNAMIS

Fig. 4 compares the observed waveforms and spectra of the 2012 and 2016 off Sumatra tsunamis. The maximum tsunami amplitudes were 0.5–1.5 cm on DARTs and 1–19 cm on tide gauges for the 2016 tsunami. The respective values were 0.5–6 and 6–40 cm for the 2012 tsunami (for the first tsunami on 2012 April 11 at 8:38, Fig. 1). Two DART records of 23227 and 23401 for the 2012 tsunami are not clear enough because of high noise level.

Fourier analysis showed that the 2016 tsunami's energy was in the period band of 4–15 min with clear peaks at ∼6 and ∼10 min (shaded area in Fig. 4b). For the 2012 tsunami, the period band was 7–24 min with peak periods at ∼10 and ∼18 min (shaded area in Fig. 4c). It can be seen that the 2012 tsunami's peak periods are noticeably longer than those of the 2016. The spectra of two tsunamis are overlaid in Fig. 4c revealing that both tsunamis have a common peak period at ∼10 min while the peak period of ∼18 min appears only in the spectrum of the 2012 tsunami (see brown-dashed and solid-black spectra in Fig. 4c, bottom).

Tsunami peak periods are influenced by the dimensions of the co-seismic seafloor deformation (i.e. the larger the seafloor deformation area, the longer the period), water depth at the source area (i.e. the larger the water depth, the shorter the period), as well as bathymetry during the propagation and around the recorded stations (Heidarzadeh & Satake 2014). The water depths at the source area are ∼5000 and ∼4400 m for the 2016 (Fig. 2) and 2012 (Fig. 1) events, respectively, indicating that water depth is equally affecting the peak periods of both events. The propagation paths between the tsunami sources and recording sites are also similar. Therefore, the longer tsunami periods of the 2012 event can be attributed to

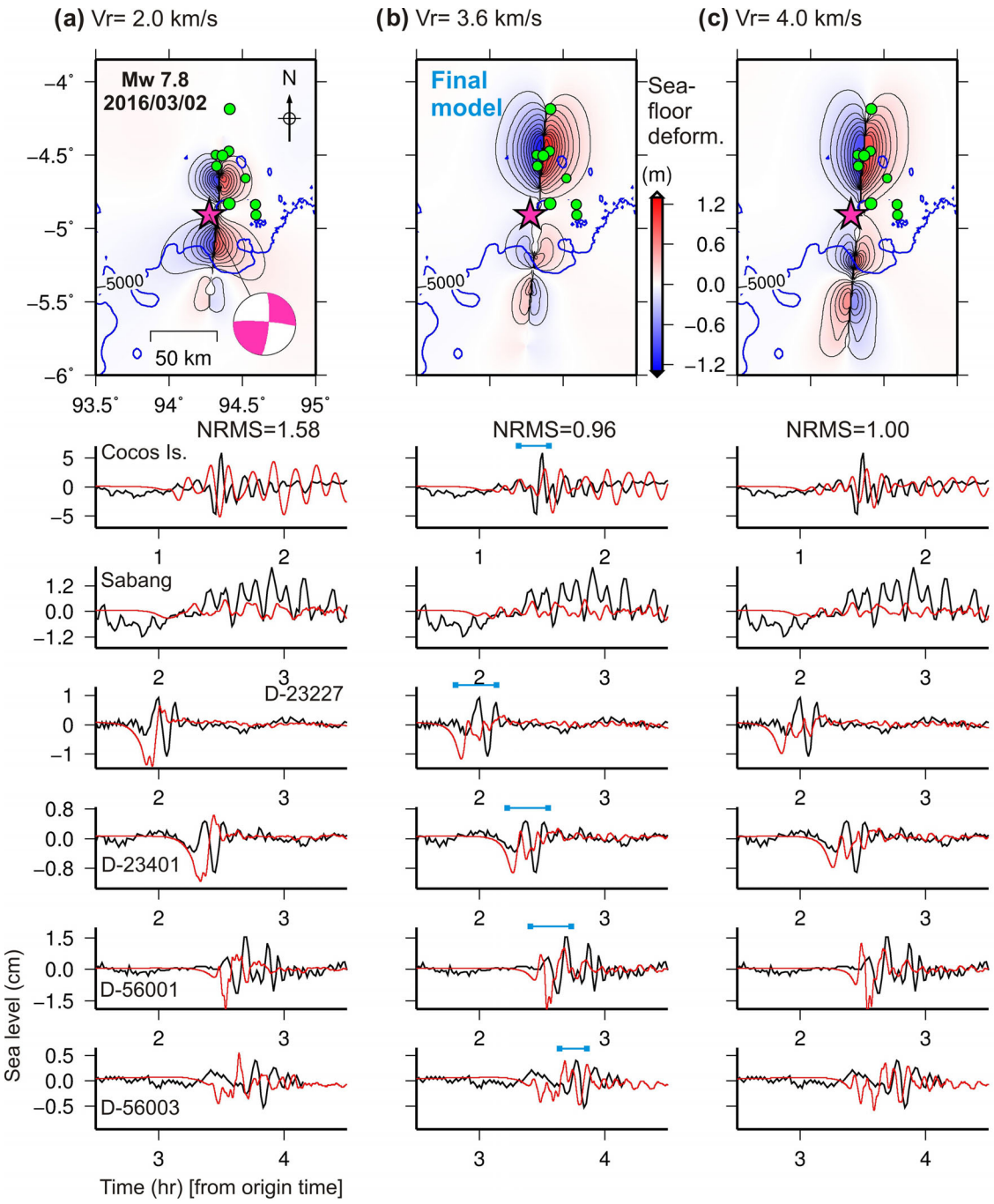

Figure 5. Results of tsunami simulations using slip distributions estimated by teleseismic waveform inversion with different rupture velocities for NS striking fault. Top row show seafloor deformations. Black and red waveforms are observed and simulated waveforms, respectively. The blue lines on top of some waveforms indicate stations and waveforms lengths used for NRMS misfit calculations.

the larger size of its seafloor deformation because it was generated by a larger earthquake (M_w 8.6) compared to the 2016 earthquake (M_w 7.8).

The peak periods of tsunami can be inverted to provide estimates of dimensions of tsunami source area (Rabinovich 1997; Rabinovich *et al.* 2008; Heidarzadeh & Satake 2013). The source dimensions of the 2016 event can be estimated from its peak periods of 6 and 10 min and by considering the water depth of ~5000 m at the source area (Fig. 2). Using eq. (5) of Heidarzadeh & Satake (2015), the source dimensions are estimated at 40 km × 70 km, which are close to the large-slip area of 48 km × 90 km determined by teleseismic inversion (previous section). Such a rough estimate looks difficult to be made for the source of the 2012 tsunami because it contains three orthogonal faults with various lengths (Meng *et al.* 2012; Wei *et al.* 2013).

5 SEISMICITY OF THE WHARTON BASIN

We studied the seismicity of the Wharton Basin using the available focal mechanism solutions of earthquakes in the period 1976–2016

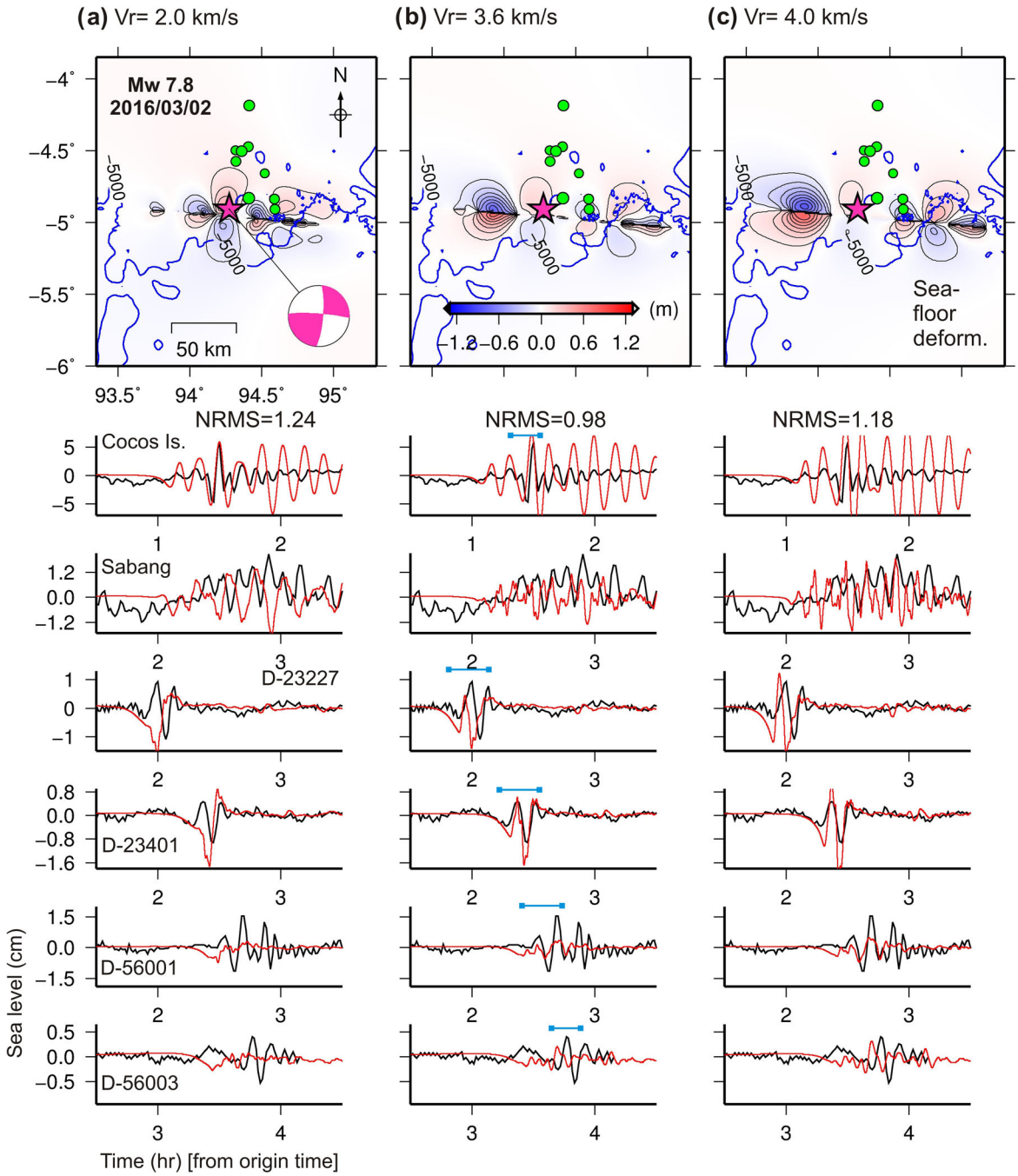

Figure 6. Results of tsunami simulations using slip distributions estimated by teleseismic waveform inversion with different rupture velocities for EW striking fault. Top row show seafloor deformations. Black and red waveforms are observed and simulated waveforms, respectively. The blue lines on top of some waveforms indicate stations and waveforms lengths used for NRMS misfit calculations.

from the GCMT catalogue (Figs 8 and 9). We divided available focal mechanism solutions into four fault-types using the criteria by Frohlich (1992). It is obvious that the strike-slip events are dominantly distributed in the Wharton Basin: while the numbers of thrust and normal earthquakes are 10 and 12, respectively, the numbers of strike-slip and oblique events are 74 and 44, respectively (Fig. 8). In other words, by excluding the oblique events, 70 per cent of the earthquakes in the Wharton Basin occurred in the form of strike-slip events. Normal-fault earthquakes occurred only in the outer-rise region near the Sunda Trench (Fig. 8c). These characteristics are consistent with previous studies (e.g. Petroy & Wiens 1989; Qin & Singh 2015). Fig. 9(a) presents the magnitude-time and cumulative frequency curves by considering only strike-slip and oblique events. The total cumulative frequency curve (black curve) reveals three sudden increase in seismicity which are attributed to the 2000 (M_w 7.9, strike-slip), 2004 (Sumatra-Andaman M_w 9.1; subduction-thrust; see Fig. 1 for location), and 2012 (M_w 8.6 and 8.2, strike-slip) events. A sharp increase in seismicity of northern Wharton Basin (latitude $> -1^\circ$) is observed following the 2012 twin events (blue curve in Fig. 8e). Wiseman & Burgmann (2012) showed that the adjacent 2004 Sumatra–Andaman M_w 9.1 earthquake loaded the Wharton Basin and has facilitated the occurrence of strike-slip events within this basin.

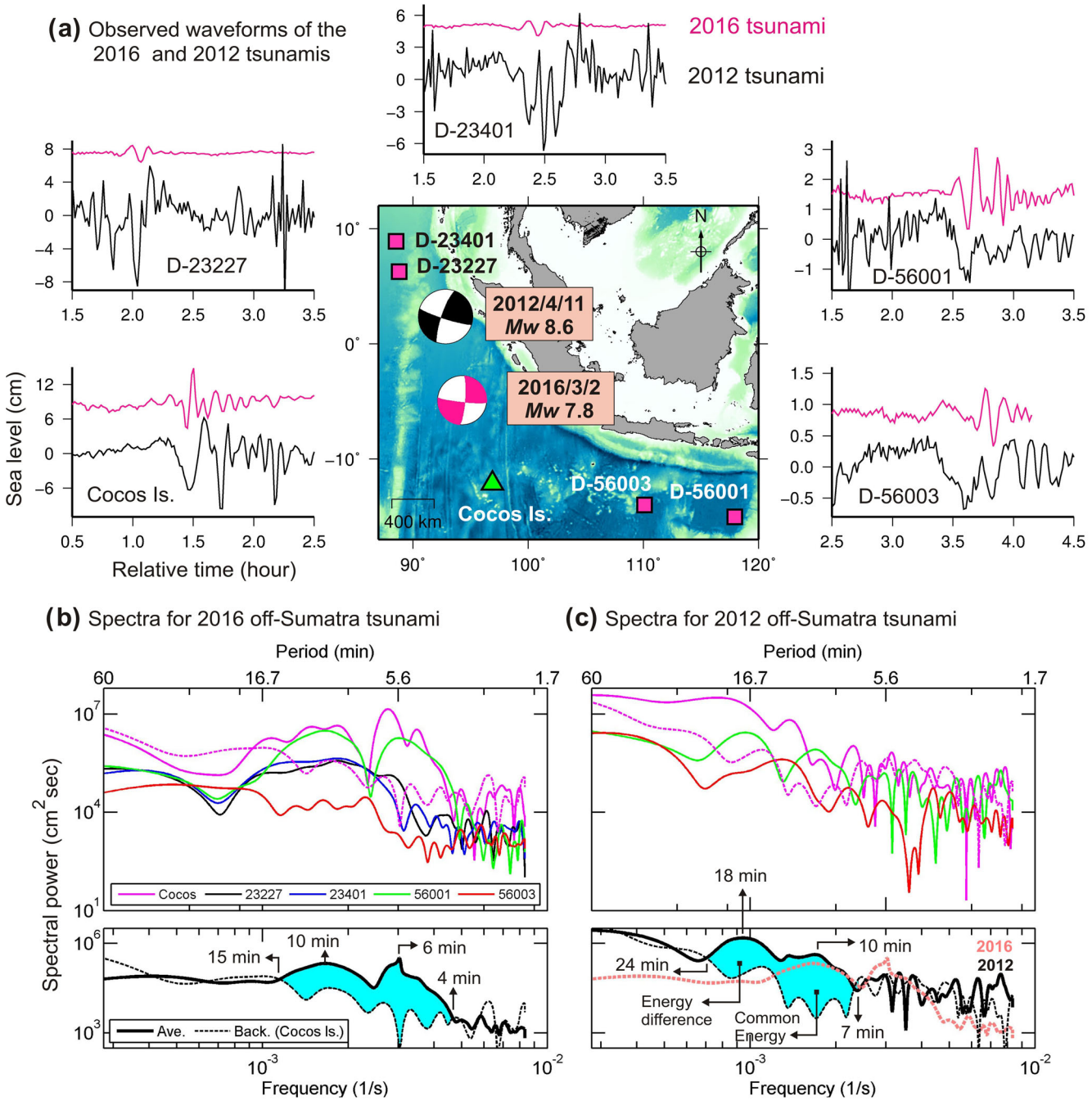

Figure 7. Comparison of the waveforms and spectra of the 2012 and 2016 off Sumatra tsunamis. (a) The observed waveforms of the 2012 and 2016 tsunamis. The time on the *x*-axis is from the origin time of the 2016 tsunami while the time of the 2012 event is shifted. (b) The spectra for the 2012 and 2016 tsunamis. The average spectra shown at the bottom row are normalized average. The term 'Back.' represents spectrum of background sea level waveforms. For the 2016 tsunami, the background spectrum is based on only the record of the Cocos Island station.

Cumulative frequency curves for various types of earthquakes and triangle diagram also indicate that most earthquakes are of strike-slip mechanism (Figs 9b and d). According to Fig. 9(c), strike-slip events provided the largest seismic moment in the Wharton Basin. It can be noted that increases in the number of strike-slip events in post 2004 and 2012 earthquakes (Figs 9a and b) are not visible in the cumulative seismic moment diagrams (Fig. 9c). A decade before the 2004 Sumatra-Andaman earthquake, strike-slip and oblique events started to increase (Fig. 9b). Further studies are necessary to examine whether this change is apparent or not.

6 CONCLUSIONS

We studied the 2016 March 2 off southwest Sumatra tsunamigenic earthquake and compared it with the 2012 April 11 event in the same region in order to achieve insights into the tsunamigenic potential of large strike-slip earthquakes in the Wharton Basin (Indian Ocean). Main results are:

(1) A source model is proposed for the March 2016 strike-slip earthquake using both teleseismic body waves and tsunami observations. The orientation of the fault was not fully constrained in

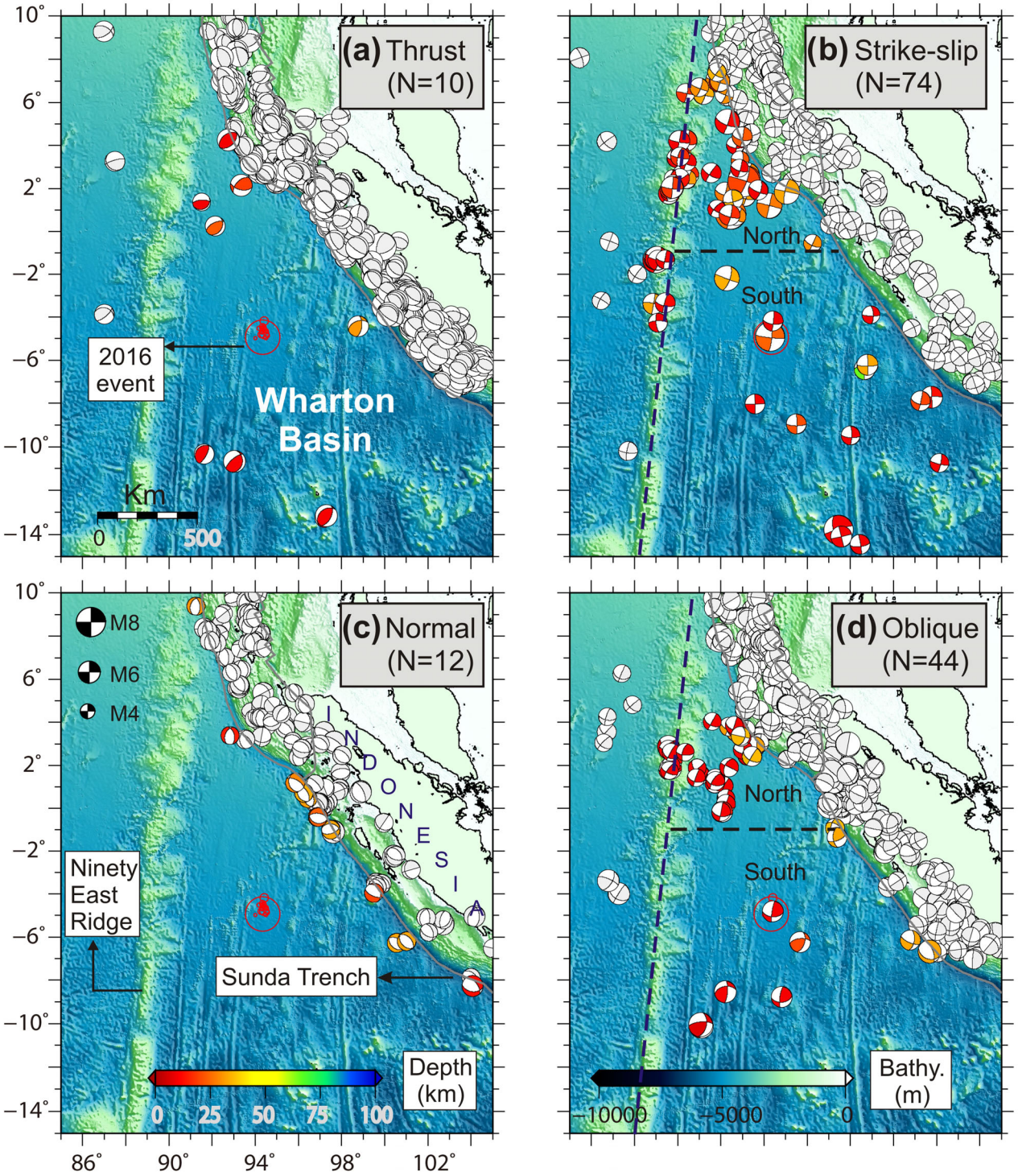

Figure 8. Focal mechanisms of earthquakes in the Wharton Basin since 1976 from GCMT catalogue for various types of earthquakes. The horizontal dashed line in panel 'c' at the latitude of –1° is the assumed border between northern and southern parts of the Wharton Basin.

this study; we obtained a group of optimum models in the range V_r = 2.8–3.6 km s^{-1} belonging to both EW and NS faults. Our best model had a V_r of 3.6 km s^{-1} from the NS-striking fault plane. The maximum and average slip values were 7.7 and 2.3 m, respectively, with source duration of 33 s. Lack of resolution to clearly distinguish between the NS and EW faults can be attributed to the small size of the tsunami and the sparse distribution of the tsunami gauges.

(2) Clear tsunami signals were recorded on DARTs and tide gauges within the Indian Ocean for both 2012 and 2016 tsunami although both had strike-slip mechanisms. The maximum tsunami amplitudes were in the ranges of 0.5–19 and 0.5–40 cm for the 2016 and 2012 tsunamis, respectively.

(3) The peak tsunami periods were 6 and 10 min for the 2016 event whereas they were 10 and 18 min for the 2012 event. The longer tsunami peak periods of the 2012 tsunami can be attributed

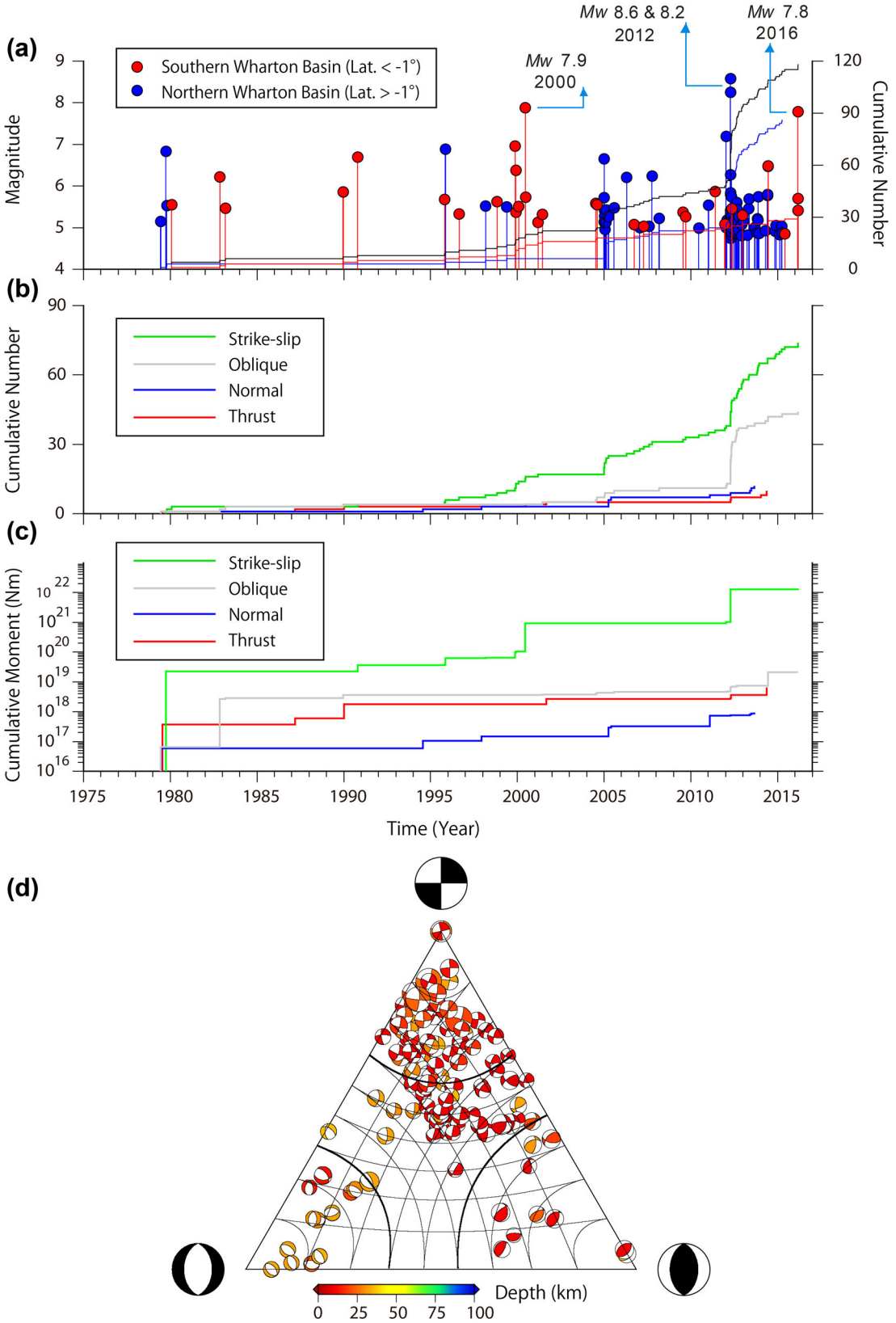

Figure 9. (a) Magnitude-time diagram (left axis) and cumulative frequency curves (right axis) for the seismicity (only strike-slip and oblique events) of northern (blue circles and curve) and southern (red circles and curve) Wharton Basin. The black curve shows the cumulative frequency curve for the entire Wharton Basin. (b) Cumulative number of earthquakes for various types of the earthquakes. (c) Cumulative seismic moment of earthquakes for various types of the earthquakes. (d) The triangular diagrams of the earthquake focal mechanisms.

to the larger size of the earthquake which generated larger seafloor deformation area.

(4) Our cumulative number and cumulative seismic-moment curves for various types of earthquakes revealed that strike-slip events dominate and the largest seismic-moment is provided by the strike-slip earthquakes in this basin.

ACKNOWLEDGEMENTS

We downloaded tide gauge data from the Intergovernmental Oceanographic Commission's website (http://www.ioc-sealevelmonitoring.org/). DART data are available at the NOAA webpage (http://nctr.pmel.noaa.gov/Dart/). We also downloaded teleseismic records of the earthquakes from Incorporated Research Institutions for Seismology website at: http://www.iris.edu/wilber3/find_event. Earthquake focal mechanism data of Global Centroid-Moment-Tensor Project (GCMT) were used in this study (http://www.globalcmt.org/). Most figures were drafted by using the GMT software (Wessel & Smith 1998). This article benefited from constructive reviews from the Editor (Dr Gael Choblet) and two anonymous reviewers. MH was funded by the Brunel University London through the Brunel Research Initiative and Enterprise Fund 2017/18 (BUL BRIEF) and also by the Great Britain Sasakawa Foundation (GBSF) grant number 5217.

REFERENCES

Abercrombie, R.E., Antolik, M. & Ekström, G., 2003. The June 2000 M_w 7.9 earthquakes south of Sumatra: deformation in the India–Australia plate, *J. geophys. Res.,* **108**(B1), doi:10.1029/2001JB000674.

Aderhold, K & Abercrombie, R.E., 2016. Seismotectonics of a diffuse plate boundary: observations off the Sumatra-Andaman trench, *J. geophys. Res.,* **121**(5), 3462–3478.

Deplus, C. *et al.* 1998. Direct evidence of active deformation in the eastern Indian oceanic plate, *Geology,* **26**(2), 131–134.

Duputel, Z., Kanamori, H., Tsai, V.C., Rivera, L., Meng, L., Ampuero, J.P. & Stock, J.M., 2012. The 2012 Sumatra great earthquake sequence, *Earth planet. Sci. Lett.,* **351,** 247–257.

Frohlich, C., 1992. Triangle diagrams: Ternary graphs to display similarity and diversity of earthquake focal mechanisms, *Phys. Earth planet. Inter.,* **75,** 193–198.

Geoware, 2011. '*The Tsunami Travel Times (TTT)*'. Available at: http://www.geoware-online.com/tsunami.html, last accessed 1 May 2011.

Gusman, A.R., Murotani, S., Satake, K., Heidarzadeh, M., Gunawan, E., Watada, S. & Schurr, B., 2015. Fault slip distribution of the 2014 Iquique, Chile, earthquake estimated from ocean-wide tsunami waveforms and GPS data, *Geophys. Res. Lett.,* **42**(4), 1053–1060.

Gusman, A.R., Satake, K. & Harada, T., 2017. Rupture process of the 2016 Wharton Basin strike-slip faulting earthquake estimated from joint inversion of teleseismic and tsunami waveforms, *Geophys. Res. Lett.,* **44,** 4082–4089.

Heidarzadeh, M. & Satake, K., 2013. The 21 May 2003 tsunami in the Western Mediterranean Sea: statistical and wavelet analyses, *Pure appl. Geophys.,* **170**(9–10), 1449–1462.

Heidarzadeh, M. & Satake, K., 2014. Excitation of basin-wide modes of the Pacific Ocean following the March 2011 Tohoku tsunami, *Pure appl. Geophys.,* **171**(12), 3405–3419.

Heidarzadeh, M. & Satake, K., 2015. New insights into the source of the Makran Tsunami of 27 November 1945 from Tsunami waveforms and coastal deformation data, *Pure appl. Geophys.,* **172**(3–4), 621–640.

Heidarzadeh, M., Gusman, A. R., Harada, T. & Satake, K., 2015. Tsunamis from the 29 March and 5 May 2015 Papua New Guinea earthquake doublet (M_w 7.5) and tsunamigenic potential of the New Britain trench, *Geophys. Res. Lett.,* **42,** 5958–5965.

Heidarzadeh, M., Murotani, S., Satake, K., Ishibe, T. & Gusman, A.R., 2016a. Source model of the 16 September 2015 Illapel, Chile M_w 8.4 earthquake based on teleseismic and tsunami data, *Geophys. Res. Lett.,* **43,** doi:10.1002/2015GL067297.

Heidarzadeh, M., Harada, T., Satake, K., Ishibe, T. & Gusman, A.R., 2016b. Comparative study of two tsunamigenic earthquakes in the Solomon Islands: 2015 M_w 7.0 normal-fault and 2013 Santa Cruz M_w 8.0 megathrust earthquakes, *Geophys. Res. Lett.,* **43**(9), 4340–4349.

IOC, IHO & BODC, 2003. Centenary Edition of the GEBCO Digital Atlas, published on CD-ROM on behalf of the Intergovernmental Oceanographic Commission and the International Hydrographic Organization as part of the General Bathymetric Chart of the Oceans, British Oceanographic Data Centre, Liverpool, UK.

Kikuchi, M. & Kanamori, H., 1991. Inversion of complex body waves—III, *Bull. seism. Soc. Am.,* **81**(6), 2335–2350.

Lay, T., Ye, L., Ammon, C.J., Dunham, A. & Koper, K.D., 2016. The 2 March 2016 Wharton Basin M_w 7.8 earthquake: high stress drop north-south strike-slip rupture in the diffuse oceanic deformation zone between the Indian and Australian Plates, *Geophys. Res. Lett.,* **43**(15), 7937–7945.

Meng, L., Ampuero, J.P., Stock, J., Duputel, Z., Luo, Y. & Tsai, V.C., 2012. Earthquake in a maze: compressional rupture branching during the 2012 M_w 8.6 Sumatra earthquake, *Science,* **337**(6095), 724–726.

Okada, Y., 1985. Surface deformation due to shear and tensile faults in a half-space, *Bull. seism. Soc. Am.,* **75,** 1135–1154.

Petroy, D.E. & Wiens, D.A., 1989. Historical seismicity and implications for diffuse plate convergence in the northeast Indian Ocean, *J. geophys. Res.,* **94**(B9), 12 301–12 319.

Qin, Y. & Singh, S.C., 2015. Seismic evidence of a two-layer lithospheric deformation in the Indian Ocean, *Nat. Commun.,* **6,** doi: 10.1038/ncomms9298.

Rabinovich, A.B., 1997. Spectral analysis of tsunami waves: separation of source and topography effects, *J. geophys. Res.,* **102**(C6), 12 663–12 676.

Rabinovich, A.B., Lobkovsky, L.I., Fine, I.V., Thomson, R.E., Ivelskaya, T.N. & Kulikov, E.A., 2008. Near-source observations and modeling of the Kuril Islands tsunamis of 15 November 2006 and 13 January 2007, *Adv. Geosci.,* **14,** 105–116.

Satake, K., 1995. Linear and nonlinear computations of the 1992 Nicaragua earthquake tsunami, *Pure appl. Geophys.,* **144,** 455–470.

Satriano, C., Kiraly, E., Bernard, P. & Vilotte, J.P., 2012. The 2012 M_w 8.6 Sumatra earthquake: Evidence of westward sequential seismic ruptures associated to the reactivation of a N-S ocean fabri, *Geophys. Res. Lett.,* **39**, L15302, doi:10.1029/2012GL052387.

Wang, D., Mori, J. & Uchide, T., 2012. Supershear rupture on multiple faults for the M_w 8.6 Off Northern Sumatra, Indonesia earthquake of April 11, 2012, *Geophys. Res. Lett.,* **39**(21), doi:10.1029/2012GL053622.

Wiseman, K. & Bürgmann, R., 2012. Stress triggering of the great Indian Ocean strike-slip earthquakes in a diffuse plate boundary zone, *Geophys. Res. Lett.,* **39**(22), doi:10.1029/2012GL053954.

Wei, S., Helmberger, D. & Avouac, J.P., 2013. Modeling the 2012 Wharton basin earthquakes off-Sumatra: complete lithospheric failure, *J. geophys. Res.,* **118**(7), 3592–3609.

Welch, P., 1967. The use of fast Fourier transform for the estimation of power spectra: a method based on time averaging over short, modified periodograms, *IEEE Trans. Audio Electroacoust,* **AE-15,** 70–73.

Wessel, P. & Smith, W.H.F., 1998. New, Improved Version of Generic Mapping Tools Released, *EOS, Trans. Am. geophys. Un.,* **79**(47), 579.

Yue, H., Lay, T. & Koper, K.D., 2012. En échelon and orthogonal fault ruptures of the 11 April 2012 great intraplate earthquakes, *Nature,* **490**(7419), 245–249.

SUPPORTING INFORMATION

Supplementary data are available at *GJI* online.

Figure S1. Results of teleseismic body-wave inversion for the 2016 March 2 Wharton Basin earthquake using rupture velocity

of 2.0 km s^{-1} showing observed (black) and computed (red) waveforms for the NS-striking fault.

Figure S2. Results of teleseismic body-wave inversion for the 2016 March 2 Wharton Basin earthquake using rupture velocity of 2.8 km s^{-1} showing observed (black) and computed (red) waveforms for the NS-striking fault.

Figure S3. Results of teleseismic body-wave inversion for the 2016 March 2 Wharton Basin earthquake using rupture velocity of 4.0 km s^{-1} showing observed (black) and computed (red) waveforms for the NS-striking fault.

Figure S4. Results of tsunami simulations for the 2016 March 2 Wharton Basin tsunami using various rupture models showing observed (black) and simulated (red) waveforms for the NS-striking fault.

Please note: Oxford University Press is not responsible for the content or functionality of any supporting materials supplied by the authors. Any queries (other than missing material) should be directed to the corresponding author for the paper.